Germanium-tin n-channel tunneling field-effect transistor: Device physics and simulation study

Yue Yang, Kain Lu Low, Wei Wang, Pengfei Guo, Lanxiang Wang, Genquan Han,[a] and Yee-Chia Yeo[a]
Department of Electrical and Computer Engineering, National University of Singapore, Singapore 117576

(Received 15 January 2013; accepted 29 April 2013; published online 20 May 2013)

We investigate germanium-tin alloy ($Ge_{1-x}Sn_x$) as a material for the design of tunneling field-effect transistor (TFET) operating at low supply voltages. Compared with Ge, $Ge_{1-x}Sn_x$ has a smaller band-gap. The reported band-gap of $Ge_{0.89}Sn_{0.11}$ is 0.477 eV, ~28% smaller than that of Ge. More importantly, $Ge_{1-x}Sn_x$ becomes a direct band-gap material when Sn composition x is higher than 0.11. By employing $Ge_{1-x}Sn_x$ in TFET, direct band-to-band tunneling (BTBT) is realized. Direct BTBT generally has higher tunneling probability than indirect BTBT. The drive current of TFET is boosted due to the direct BTBT and the reduced band-gap of $Ge_{1-x}Sn_x$. Device simulations show that the drive current and subthreshold swing S characteristics of $Ge_{1-x}Sn_x$ TFETs with x ranging from 0 to 0.2 are improved by increasing the Sn composition x. For $Ge_{0.8}Sn_{0.2}$ TFET, sub-60 mV/decade S is achieved at a high current level of ~8 μA/μm. For x higher than 0.11, $Ge_{1-x}Sn_x$ TFETs show higher on-state current I_{ON} compared to Ge TFET at a supply voltage of 0.3 V. $Ge_{1-x}Sn_x$ alloy is a potential candidate for high performance TFET composed of group IV materials. © *2013 AIP Publishing LLC*. [http://dx.doi.org/10.1063/1.4805051]

I. INTRODUCTION

The tunneling field-effect transistor (TFET) is a promising device candidate to overcome the 60 mV/decade subthreshold swing S limitation of the conventional metal-oxide-semiconductor field-effect transistor (MOSFET). The TFET exploits the phenomenon of gate modulated band-to-band tunneling (BTBT) to achieve a steep S and a high on-state current I_{ON} to off-state current I_{OFF} ratio at a low supply voltage V_{DD}. TFETs with S below 60 mV/decade have been demonstrated experimentally,[1–6] but achieving I_{ON} comparable with that of state-of-the-art high-performance complementary metal-oxide semiconductor (CMOS) is challenging. There have been many research efforts directed at improving I_{ON} of TFETs, and one effective approach employs band-gap engineering. Materials with smaller band-gaps, such as germanium (Ge), indium gallium arsenide (InGaAs), and indium arsenide (InAs), have been used in the tunneling regions of TFETs to boost I_{ON}.[5–12] In addition, direct BTBT is preferred for TFET operation, as tunneling of electrons from valence band (E_V) to conduction band at Γ-point ($E_{C,\Gamma}$) without a change in momentum gives rise to a higher I_{ON} than indirect BTBT.[13–15] Therefore, a direct band-gap material is desired for use in TFET device design. Thus, III-V materials are very suitable for realizing high I_{ON} in TFETs.

It should be noted that the band structure of Ge can be modified by introducing strain,[16] and Ge becomes a direct band-gap material under high tensile strain. In addition, it is also possible to incorporate substitutional tin (Sn) in Ge to form germanium-tin ($Ge_{1-x}Sn_x$) alloy. By tuning the Sn composition x, $Ge_{1-x}Sn_x$ can be a direct material with a smaller band-gap than Ge.[17–36] Moreover, as a group IV material, $Ge_{1-x}Sn_x$ may be more process compatible or more easily integrated with silicon-based CMOS technology as compared to III-V compound semiconductors. These considerations make $Ge_{1-x}Sn_x$ an attractive material for TFET device design.

In this work, the device physics of $Ge_{1-x}Sn_x$ n-channel TFETs with x varying from 0 to 0.2 is investigated. Based on electronic band structures calculated by non-local Empirical Pseudopotential Method (EPM), the BTBT related material parameters of $Ge_{1-x}Sn_x$ alloys are obtained. Two-dimensional (2D) technology computer-aided design (TCAD) simulation study on $Ge_{1-x}Sn_x$ TFET is also performed for the first time. The objective is to examine the potential of high quality $Ge_{1-x}Sn_x$ with high Sn composition, which may be realized in the future, for application in TFETs. Both the direct BTBT from E_V to $E_{C,\Gamma}$ and the indirect BTBT from E_V to conduction band at L-point ($E_{C,L}$) are calculated, which are denoted by "direct Γ-Γ BTBT" and "indirect Γ-L BTBT," respectively. Simulation results show that by employing $Ge_{1-x}Sn_x$ in TFETs, an enhancement in drive current and S, as compared with Ge TFET, can be achieved.

II. EXTRACTION AND CALCULATION OF MATERIAL PARAMETERS

The band structures of $Ge_{1-x}Sn_x$ alloys have been studied both theoretically[17–23] and experimentally,[24–36] and the transistor fabrication has been demonstrated.[37–40] The reported Sn compositional dependence of band-gaps at Γ and L-point, denoted as $E_{G,\Gamma}$ and $E_{G,L}$, respectively, are shown in Fig. 1(a). The crossover from indirect-to-direct band-gap occurs at $x = 0.06 - 0.11$.[33–36] In this work, the crossover from indirect band-gap is assumed to be at $x = 0.11$ according to Ref. 35. Based on the values of $E_{G,L}$

[a]Authors to whom correspondence should be addressed. Electronic addresses: hangenquan@ieee.org and yeo@ieee.org. Telephone: +65 6516-2298. Fax: +65 6779-1103.

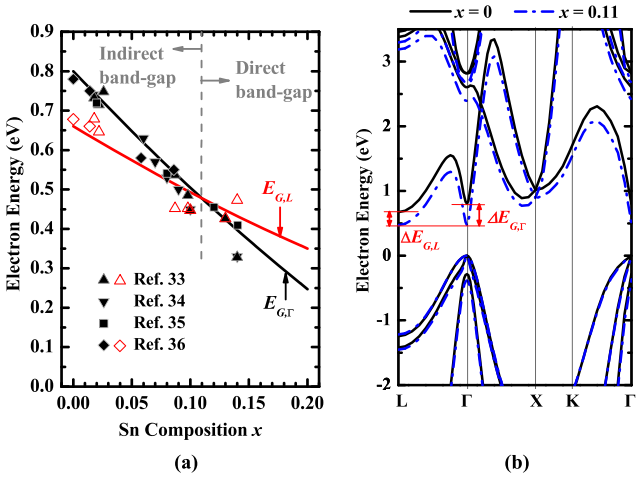

FIG. 1. (a) Composition dependence of $Ge_{1-x}Sn_x$ band-gap at Γ-valley ($E_{G,\Gamma}$) and L-valley ($E_{G,L}$) for $Ge_{1-x}Sn_x$ alloy. Symbols are experimental data and the lines are obtained from EPM calculations. For $Ge_{1-x}Sn_x$ alloys with Sn composition x below 0.11, the conduction band minimum is at L-point, and the alloy is an indirect band-gap material. For x higher than 0.11, $Ge_{1-x}Sn_x$ is a direct band-gap material since the conduction band minimum is located at Γ-point. (b) Full band E-k dispersion for Ge and $Ge_{0.89}Sn_{0.11}$. As Sn composition increases, $Ge_{1-x}Sn_x$ alloy transits from indirect to direct band-gap at around $x = 0.11$. The differences in band-gaps at Γ-point and L-point are highlighted as $\Delta E_{G,\Gamma}$ and $\Delta E_{G,L}$.

and $E_{G,\Gamma}$ from Ref. 35, the form factors used in non-local-EPM[41] were adjusted to reproduce the full band structures of $Ge_{1-x}Sn_x$. The accuracy of the EPM results depends on the match with reported experimental data and the details of the calibration or the EPM calculation can be found in Ref. 42. Due to the introduction of Sn, $E_{G,\Gamma}$ and $E_{G,L}$ of $Ge_{1-x}Sn_x$ decrease as Sn composition increases [see Fig. 1(a)]. By varying x from 0 to 0.2, the band-gap reduction at Γ-point ($\Delta E_{G,\Gamma}$) is more pronounced than that at L-point ($\Delta E_{G,L}$), causing $Ge_{1-x}Sn_x$ alloy to become a direct band-gap material when x is 0.11 or larger. This can be observed from a comparison between the full band structures of Ge and $Ge_{0.89}Sn_{0.11}$, as shown in Fig. 1(b).

In order to perform a simulation of the electrical characteristics of $Ge_{1-x}Sn_x$ TFETs, material parameters of $Ge_{1-x}Sn_x$ such as density-of-states (DOS) effective masses of electrons and holes, intrinsic carrier concentrations, and tunneling reduced masses are needed. These parameters can be calculated based on the effective masses extracted from the full band E-k plots obtained by EPM.[42]

The electron effective masses (transverse effective mass $m^*_{e,t}$ and longitudinal effective mass $m^*_{e,l}$ in L-valley, isotropic effective mass $m^*_{e,\Gamma}$ in Γ-valley) and hole effective masses (heavy hole effective mass m^*_{hh} and light hole effective mass m^*_{lh}) are extracted directly from the band edges using a parabolic line fit. The electron DOS effective masses at Γ-valley and L-valley ($m^*_{DOS,\Gamma}$ and $m^*_{DOS,L}$, respectively) are calculated as $m^*_{DOS,\Gamma} = m^*_{e,\Gamma}$ and $m^*_{DOS,L} = 4^{2/3}(m^*_{e,t})^{2/3}(m^*_{e,l})^{1/3}$. The values of $m^*_{DOS,\Gamma}$ and $m^*_{DOS,L}$ for $Ge_{1-x}Sn_x$ with x ranging from 0 to 0.2 are presented in Fig. 2(a). $m^*_{DOS,\Gamma}$ becomes smaller with increasing Sn composition, while $m^*_{DOS,L}$ shows negligible dependence on Sn composition. For valence band, Luttinger parameters γ_1, γ_2, and γ_3 are fitted from full band E-k by EPM.[42] The hole DOS effective mass $m^*_{DOS,h}$ is

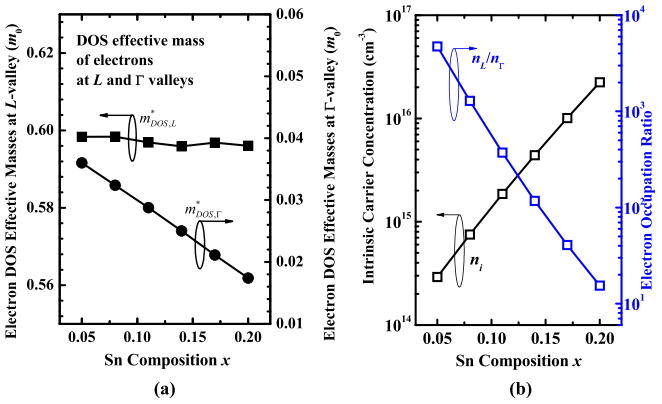

FIG. 2. (a) The DOS electron effective mass in the L-valley ($m^*_{DOS,L}$) is larger than the one in the Γ-valley ($m^*_{DOS,\Gamma}$) for $Ge_{1-x}Sn_x$ alloys with various x. (b) The intrinsic carrier concentration and electron occupation ratio versus Sn composition. For $Ge_{1-x}Sn_x$ with $x > 0.11$, although the conduction band minimum at the Γ-valley is lower than the one at the L-valley, there are more electrons in L-valley than Γ-valley.

calculated based on spherically averaged heavy hole (m^*_{HH}) and light hole (m^*_{LH}) effective masses as $m^*_{DOS,h} = [(m^*_{HH})^{3/2} + (m^*_{LH})^{3/2}]^{2/3}$, where $m^*_{HH}/m_0 = [\gamma_1(1-(6\gamma_3+4\gamma_2)/5\gamma_1)]^{-1}$ and $m^*_{LH}/m_0 = [\gamma_1(1+(6\gamma_3+4\gamma_2)/5\gamma_1)]^{-1}$.[43]

The intrinsic carrier concentration n_i is given by

$$n_i = N_{C,L} \cdot e^{-\frac{E_{C,L}-E_i}{kT}} + N_{C,\Gamma} \cdot e^{-\frac{E_{C,\Gamma}-E_i}{kT}} = N_V \cdot e^{-\frac{E_i-E_V}{kT}}, \quad (1)$$

where E_i is intrinsic Fermi level, $N_{C,L} = 2(2\pi \cdot m^*_{DOS,L} kT/h^2)^{3/2}$, $N_{C,\Gamma} = 2(2\pi \cdot m^*_{DOS,\Gamma} kT/h^2)^{3/2}$, $N_V = 2(2\pi \cdot m^*_{DOS,h} kT/h^2)^{3/2}$, k is the Boltzmann constant, T is temperature in degrees Kelvin, and h is the Planck's constant. Therefore, n_i can be rewritten as

$$n_i = N_V^{\frac{1}{2}}\left(N_{C,L} \cdot e^{-\frac{E_{G,L}}{kT}} + N_{C,\Gamma} \cdot e^{-\frac{E_{G,\Gamma}}{kT}}\right)^{\frac{1}{2}}. \quad (2)$$

The ratio of the electron concentration n_L at the L-valley to the electron concentration n_Γ at the Γ-valley in $Ge_{1-x}Sn_x$ alloy is, therefore,

$$\frac{n_L}{n_\Gamma} = \frac{N_{C,L} \cdot e^{-\frac{E_{G,L}-E_i}{kT}}}{N_{C,\Gamma} \cdot e^{-\frac{E_{G,\Gamma}-E_i}{kT}}} = \frac{N_{C,L}}{N_{C,\Gamma}} \cdot e^{-\frac{E_{G,L}-E_{G,\Gamma}}{kT}}. \quad (3)$$

The values of n_i and the ratio n_L/n_Γ at various Sn compositions are shown in Fig. 2. The increase of n_i with x is mainly due to the decrease of $E_{G,L}$ and $E_{G,\Gamma}$ with increasing Sn composition. It should be noted that the electron population at L-valley is a few orders of magnitude larger than that at Γ-valley for $0 \le x \le 0.2$. The larger electron population at L-valley is due to the larger DOS electron effective mass. The electron occupation ratio n_L/n_Γ decreases as x increases, which is consistent with Ref. 23.

The tunneling reduced mass m^*_r is an important material parameter in the calculation of BTBT current. For $Ge_{1-x}Sn_x$ TFET, both direct Γ-Γ and indirect Γ-L BTBT current components need to be calculated. Direct tunneling reduced mass $m^*_{r,\Gamma}$ and indirect tunneling reduced mass $m^*_{r,L}$ are obtained using[11,14,44]

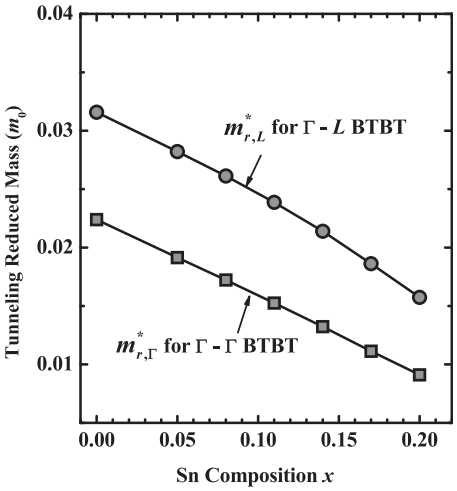

FIG. 3. Tunneling reduced masses for Γ-Γ BTBT ($m^*_{r,\Gamma}$) and Γ-*L* BTBT ($m^*_{r,L}$) decrease as Sn composition increases.

$$m^*_{r,\Gamma} = (m^*_{e,\Gamma} \times m^*_{lh})/(m^*_{e,\Gamma} + m^*_{lh}), \tag{4}$$

and

$$m^*_{r,L} = (m^*_{e,t} \times m^*_{lh})/(m^*_{e,t} + m^*_{lh}), \tag{5}$$

respectively. The dependence of $m^*_{r,\Gamma}$ and $m^*_{r,L}$ on Sn composition is shown in Fig. 3. $m^*_{r,\Gamma}$ is smaller than $m^*_{r,L}$ at the same Sn composition. As discussed later, this contributes to a larger probability of direct Γ-Γ BTBT as compared with indirect Γ-*L* BTBT. It is also found that both $m^*_{r,\Gamma}$ and $m^*_{r,L}$ decrease with increasing Sn composition.

Other material parameters, such as relative permittivity and mass density, are calculated by linear interpolation between the values of Ge and Sn. The electron affinity of $Ge_{1-x}Sn_x$ is assumed to be 4.05 eV. The $Ge_{1-x}Sn_x$ material parameters used in this work are summarized in Table I.

III. SIMULATION METHODOLOGY

The simulation of $Ge_{1-x}Sn_x$ TFETs was performed using our in-house 2D-TCAD simulator which implements a physics-based non-local BTBT algorithm.[45] The algorithm automatically identifies the tunneling paths using a 2D extension of Wentzel–Kramers–Brillouin method,[46–48] and the tunneling probability along each path is obtained by integration. The calculation of BTBT carrier generation rate is based on the tunneling probability, and the electron concentration at the starting nodes and the concentration of empty states at the ending nodes of the tunneling paths. The generation rate is then captured in the current continuity equation. The current continuity and Poisson equations are self-consistently solved using Newton's iteration method. The algorithm is designed to be robust, and the converged electrical results have been shown to be mesh grid independent.[45] In the TCAD device simulation, both direct Γ-Γ BTBT and indirect Γ-*L* BTBT were considered simultaneously.

The direct Γ-Γ BTBT generation rate (G^{dir}_{BTBT}) is obtained by an integration in energy scale of the BTBT generation rate for all the tunneling paths. The generation rate contributed by each tunneling path is calculated based on the direct tunneling probability (T^{dir}_{Tunnel}) and carrier concentrations at the starting and ending nodes of the tunneling path,[45]

$$G^{dir}_{BTBT} = \int_{E_{C,\Gamma\min}}^{E_{V,\max}} \frac{4\pi q m^*_{DOS,\Gamma} kT}{h^3} \frac{n_C p_V - n_i^2}{(n_C + n_i)(p_V + n_i)} W \cdot T^{dir}_{tunnel} \cdot dE, \tag{6}$$

$$T^{dir}_{tunnel} = e^{(-2\cdot\int|\kappa|dr)}, \text{ with } \kappa = \frac{2\pi}{h}\sqrt{2m^*_{r,\Gamma}[V(r) - E]}, \tag{7}$$

where E is carrier energy, W is the width of tunnel path, p_V is the hole concentration at the starting node of tunneling at $E = E_V$ at source side, n_C is the electron concentration at the ending node at $E = E_{C,\Gamma}$ in the channel region, κ is the imaginary part of the electron wave vector in the forbidden bandgap, and $V(r) - E$ is the barrier height at position r. The integration in Eq. (6) is performed from the minimum $E_{C,\Gamma}$ ($E_{C,\Gamma min}$) to the maximum E_V ($E_{V,max}$).

The indirect Γ-*L* BTBT is a phonon-assisted tunneling process, which involves a change in carrier momentum from Γ-point to *L*-point. The indirect BTBT process has to involve phonon for momentum conservation, and the BTBT generation rate is reduced by an attenuating pre-factor.[15] The attenuating pre-factor α_{ph} is used to capture the reduction in BTBT generation rate due to the phonon scattering effect. In this work, we take the ratio of direct BTBT generation rate to indirect BTBT generation rate from Kane's model to obtain α_{ph},[13,49]

TABLE I. Summary of material parameters used in TCAD simulation.

	Band-gap (eV)				Electron DOS mass (m_0)			Tunneling reduced mass (m_0)	
x	$E_{G,L}$	$E_{G,\Gamma}$	Relative permittivity	Mass density (kg/cm^3)	$m^*_{DOS,L}$	$m^*_{DOS,\Gamma}$	Hole DOS mass (m_0) $m^*_{DOS,h}$	$m^*_{r,\Gamma}$	$m^*_{r,L}$
0.00	0.660	0.800	16.00	5.330	0.6	0.041	0.370	0.0224	0.0316
0.05	0.573	0.648	16.40	5.352	0.598	0.036	0.366	0.0191	0.0282
0.08	0.524	0.561	16.64	5.365	0.598	0.032	0.361	0.0172	0.0261
0.11	0.477	0.477	16.88	5.377	0.597	0.029	0.358	0.0152	0.0239
0.14	0.433	0.397	17.12	5.391	0.596	0.025	0.356	0.0132	0.0214
0.17	0.390	0.318	17.36	5.404	0.597	0.021	0.351	0.0111	0.0186
0.20	0.351	0.247	17.60	5.417	0.596	0.017	0.349	0.0091	0.0157

$$\alpha_{ph} = \frac{(1+2N_{TA})D_{TA}^2}{\rho \cdot \varepsilon_{TA}} \frac{9[m_{e,t}^* \cdot m_{e,t}^* \cdot m_{e,l}^* \cdot m_{DOS,h}^{*\,3}]^{1/2}(q\xi)^{1/2}}{2^{17/4}\pi \cdot h^{1/2}(m_{r,L}^*)^{7/4}(E_{G,L})^{5/4}}, \quad (8)$$

where mass density ρ and acoustic phonon energy ε_{TA} are calculated by linear interpolation between Ge and Sn, N_{TA} is phonon occupation number and expressed as $1/(e^{\varepsilon_{TA}/kT}-1)$, D_{TA} is constant deformation potential, and the value for Ge, 8×10^{-9} eV/m, is used,[14] q is the charge of an electron, and ξ is average electric field over the length of the tunneling path. Note that only transverse acoustic phonons are taken into account since they contribute most in the phonon-assisted BTBT due to their highest occupation number and the smallest phonon energy.[14,50]

Therefore, the indirect G-L BTBT generation rate (G_{BTBT}^{ind}) is calculated using

$$G_{BTBT}^{ind} = \int_{E_{C,L\min}}^{E_{V,\max}} \alpha_{ph} \frac{4\pi q m_{DOS,L}^* kT}{h^3} \frac{n_C p_V - n_i^2}{(n_C+n_i)(p_V+n_i)} \times W \cdot T_{tunnel}^{ind} \cdot dE, \quad (9)$$

$$T_{tunnel}^{ind} = e^{(-2\cdot\int|\kappa|dr)}, \text{ with } \kappa = \frac{2\pi}{h}\sqrt{2m_{r,L}^*[V(r)-E]}, \quad (10)$$

where T_{tunnel}^{ind} is the indirect tunneling probability. The integration in Eq. (9) is performed from the minimum $E_{C,L}$ ($E_{C,\Gamma min}$) to $E_{V,max}$. In Ge, G_{BTBT}^{ind} is around 2 orders of magnitude lower than G_{BTBT}^{dir} for electric field in the order of a few MV/cm, which agrees with previous simulation work.[14,51]

Besides the non-local BTBT algorithm discussed above, the device simulator also implements the Fermi-Dirac statistics model, a doping-dependent mobility model,[52,53] the high field velocity saturation model,[52] and the Auger[54,55] and Shockley-Read-Hall[56] generation-recombination models. The device structure and key parameters of the simulated double-gate (DG) $Ge_{1-x}Sn_x$ (001) n-channel TFET are shown in Fig. 4(a). It should be noted that the quantum confinement is not taken into account due to the constraints of our simulator. In this work, a body thickness larger than the Bohr radius of Ge was used, and quantum effects may be neglected.

It should be noted that the state-of-the-art $Ge_{1-x}Sn_x$ material with high Sn concentration (e.g., $x>0.10$) is not defect-free at present. Further improvements in growth technology and material quality may be expected in the future. The GeSn material in this work is assumed to be free of bulk defects or traps. Thus, trap-assisted tunneling is not considered in the device simulation, and we are effectively examining the upper bound of the electrical performance of GeSn TFETs. In the presence of traps, the off-state leakage current and subthreshold swing would be substantially higher due to trap-assisted tunneling.

IV. ANALYSIS AND DISCUSSION

Device simulation of $Ge_{1-x}Sn_x$ TFET with various Sn compositions was performed using the device structure shown in Fig. 4(a). $Ge_{1-x}Sn_x$ TFETs with Sn composition of 0.05 and 0.14 are studied, which represent the cases of using indirect and direct E_G materials, respectively. Figs. 4(b) and 4(c) show the band diagrams of $Ge_{0.95}Sn_{0.05}$ and $Ge_{0.86}Sn_{0.14}$ TFETs near the surface along X-axis at $V_{GS}=V_{DS}=0.3$ V. For $Ge_{0.95}Sn_{0.05}$ TFET, $E_{C,L}$ is lower than $E_{C,\Gamma}$, and the tunneling distance from E_V at the source side to $E_{C,L}$ in the channel d_{ind} is shorter than that from E_V at the source side to $E_{C,\Gamma}$ in the channel d_{dir}. For $Ge_{0.86}Sn_{0.14}$ TFET, $E_{C,\Gamma}$ is lower than $E_{C,L}$, causing a smaller d_{dir} than d_{ind}.

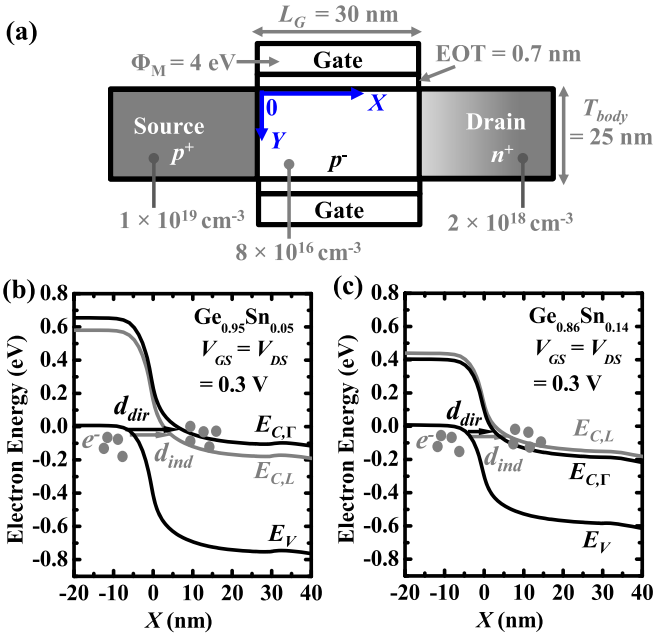

FIG. 4. (a) Schematic showing device structure of DG $Ge_{1-x}Sn_x$ TFET. (b) Band diagram near surface along X-axis of $Ge_{0.95}Sn_{0.05}$ TFET at $V_{GS}=V_{DS}=0.3$ V. Since $E_{C,L}$ is lower than $E_{C,\Gamma}$, the tunneling distance from E_V at the source side to $E_{C,L}$ in the channel d_{ind} (denoted by gray arrow) is shorter than that from E_V at the source side to $E_{C,\Gamma}$ in the channel d_{dir} (denoted by black arrow). (c) Band diagram near surface along X-axis of $Ge_{0.86}Sn_{0.14}$ TFET at $V_{GS}=V_{DS}=0.3$ V. Since $E_{C,\Gamma}$ is lower than $E_{C,L}$, d_{dir} is shorter than d_{ind}.

Figs. 5 and 6 show the spatial distribution of G_{BTBT}^{ind}, G_{BTBT}^{dir}, and total generation BTBT rate G_{BTBT}^{tot} for $Ge_{0.95}Sn_{0.05}$ and $Ge_{0.86}Sn_{0.14}$ TFETs, respectively, at $V_{GS}=V_{DS}=0.3$ V. For $Ge_{0.95}Sn_{0.05}$ TFET, the contour plots of G_{BTBT}^{ind} and G_{BTBT}^{dir} are shown in Figs. 5(a) and 5(b), respectively. By comparing Figs. 5(a) and 5(b), we observe that the magnitude of G_{BTBT}^{dir} is larger than G_{BTBT}^{ind} due to the higher tunneling probability of direct Γ-Γ BTBT. G_{BTBT}^{tot} is obtained by summing up the indirect Γ-L and direct Γ-Γ BTBT components [Fig. 5(c)]. It is found that G_{BTBT}^{dir} is the dominant component in G_{BTBT}^{tot} at the given bias. Figs. 6(a) and 6(b) show the G_{BTBT}^{ind} and G_{BTBT}^{dir}, respectively, for $Ge_{0.86}Sn_{0.14}$ TFET. $Ge_{0.86}Sn_{0.14}$ is direct band-gap material with $E_{C,\Gamma}$ lower than $E_{C,L}$. G_{BTBT}^{tot} is dominated by Γ-Γ BTBT component for $Ge_{0.86}Sn_{0.14}$ TFET [Fig. 6(c)], which is the same as the case of $Ge_{0.95}Sn_{0.05}$ TFET. Comparing Figs. 5(c) and 6(c), we can observe that under the same bias condition, the magnitude of G_{BTBT}^{tot} for $Ge_{0.86}Sn_{0.14}$ TFET is larger than that for $Ge_{0.95}Sn_{0.05}$ TFET. This is mainly due to the enhanced G_{BTBT}^{dir} caused by the smaller $E_{G,\Gamma}$ when x is higher.

The simulated I_{DS}-V_{GS} curves for $Ge_{0.95}Sn_{0.05}$ and $Ge_{0.86}Sn_{0.14}$ TFETs with direct Γ-Γ and indirect Γ-L

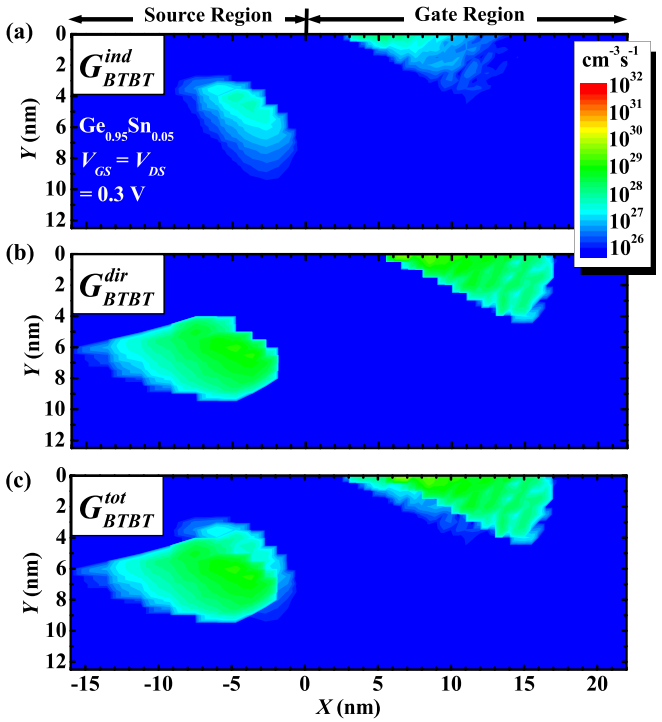

FIG. 5. Spatial distributions of (a) G_{BTBT}^{ind}, (b) G_{BTBT}^{dir}, and (c) G_{BTBT}^{tot} for $Ge_{0.95}Sn_{0.05}$ TFET at $V_{GS} = V_{DS} = 0.3$ V. As the double-gate device is symmetrical about a mirror line at $Y = 12.5$ nm, only the upper half body ($0 < Y < 12.5$ nm) is shown.

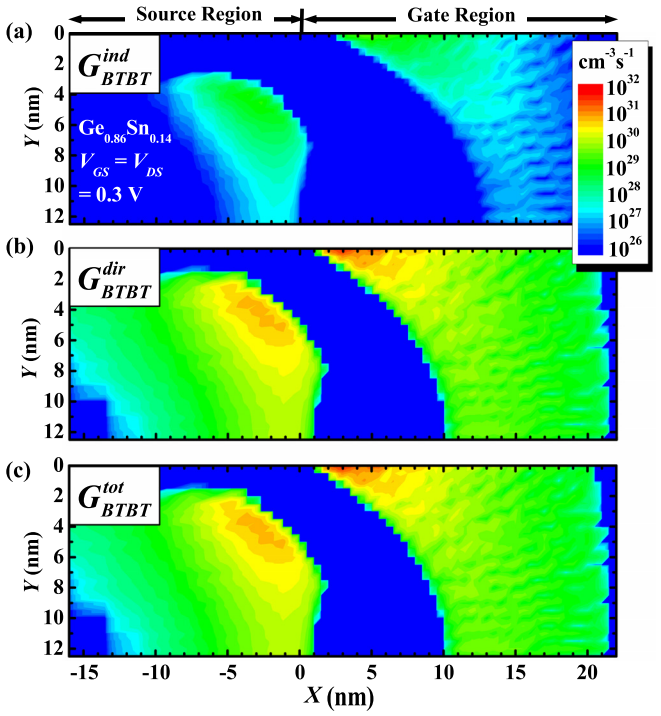

FIG. 6. Spatial distributions of (a) G_{BTBT}^{ind}, (b) G_{BTBT}^{dir}, and (c) G_{BTBT}^{tot} for $Ge_{0.86}Sn_{0.14}$ TFET at $V_{GS} = V_{DS} = 0.3$ V. As the double-gate device is symmetrical about a mirror line at $Y = 12.5$ nm, only the upper half body ($0 < Y < 12.5$ nm) is shown. The magnitude of G_{BTBT}^{tot} for $Ge_{0.86}Sn_{0.14}$ TFET is larger than that for $Ge_{0.95}Sn_{0.05}$ TFET shown in Fig. 5(c).

tunneling current components are plotted in Fig. 7. For $Ge_{0.95}Sn_{0.05}$ TFET [Fig. 7(a)], the voltage V_{ind} at which the onset of indirect Γ-*L* BTBT occurs is lower than the voltage V_{dir} at which the onset of direct Γ-Γ BTBT occurs. This is due to the smaller value of $E_{G,L}$ as compared with $E_{G,\Gamma}$. Therefore, indirect BTBT current dominates the total current for $V_{ind} < V_{GS} < V_{dir}$. For $V_{GS} > V_{dir}$, both indirect and direct BTBT take place, and the direct Γ-Γ BTBT dominates the total current due to G_{BTBT}^{dir} being larger than G_{BTBT}^{ind}. On the other hand, for $Ge_{0.86}Sn_{0.14}$ TFET [Fig. 7(b)], $E_{C,\Gamma}$ is lower than $E_{C,L}$, V_{dir} is lower than V_{ind}, and the direct BTBT dominates the total tunneling current for $V_{GS} > V_{dir}$. For $Ge_{1-x}Sn_x$ TFETs with both direct and indirect E_G, simulations indicate that the direct Γ-Γ BTBT contributes more to the total drive current once it occurs ($V_{GS} > V_{dir}$) due to the larger value of G_{BTBT}^{dir} in direct Γ-Γ BTBT compared with G_{BTBT}^{ind} in indirect Γ-*L* BTBT. This is due to the higher tunneling probability for direct BTBT than indirect BTBT.

Fig. 8(a) shows the I_{DS}-V_{GS} characteristics of $Ge_{1-x}Sn_x$ TFETs with x ranging from 0 to 0.2. The drive current of $Ge_{1-x}Sn_x$ TFETs increases with Sn composition at a fixed V_{GS}. The V_{GS} at which the drain current rises steeply reduces with increasing Sn composition, and this is related to the band-gap reduction. It is also observed that the leakage floor of $Ge_{1-x}Sn_x$ TFETs increases with Sn composition. The leakage floor is determined by the leakage current of reverse biased p-i-n junction, which is higher for a smaller band-gap.

S obtained at each V_{GS} is defined to be $dV_{GS}/d(\log I_{DS})$ and may also be referred to as Point *S*. Point *S* versus I_{DS} curves for $Ge_{1-x}Sn_x$ TFETs with x ranging from 0 to 0.2 are plotted in Fig. 8(b). By incorporation Sn into Ge, *S* of TFET is improved significantly. The reduction of *S* values is more obvious for $Ge_{1-x}Sn_x$ TFETs with direct band-gap ($x = 0.11$, 0.14, 0.17, and 0.2). More importantly, the maximum I_{DS} with sub-60 mV/decade *S* becomes higher as Sn composition increases. The improvement of *S* characteristics for $Ge_{1-x}Sn_x$ TFETs is due to the following reasons. First, as x is larger than 0.11, $Ge_{1-x}Sn_x$ becomes a direct band-gap material, and I_{DS} is dominated by direct BTBT. Direct BTBT results in a

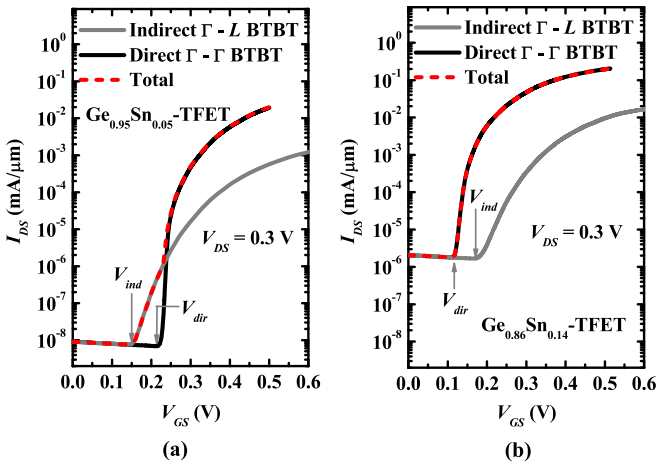

FIG. 7. (a) Simulated I_{DS}-V_{GS} for $Ge_{0.95}Sn_{0.05}$ TFET. V_{ind} is lower than V_{dir} since $E_{G,L}$ is smaller than $E_{G,\Gamma}$. As V_{GS} is larger than V_{ind}, BTBT from E_V at source side to $E_{C,L}$ occurs. However, at $V_{GS} > V_{dir}$, BTBT from E_V to $E_{C,\Gamma}$ dominates the tunneling current. (b) Simulated I_{DS}-V_{GS} for $Ge_{0.86}Sn_{0.14}$ TFET. V_{dir} is lower than V_{ind} since $E_{G,\Gamma}$ is smaller than $E_{G,L}$. As $V_{GS} > V_{dir}$, BTBT occurs from E_V at source side to $E_{C,\Gamma}$ and dominates the drive current once V_{GS} reaches V_{dir}.

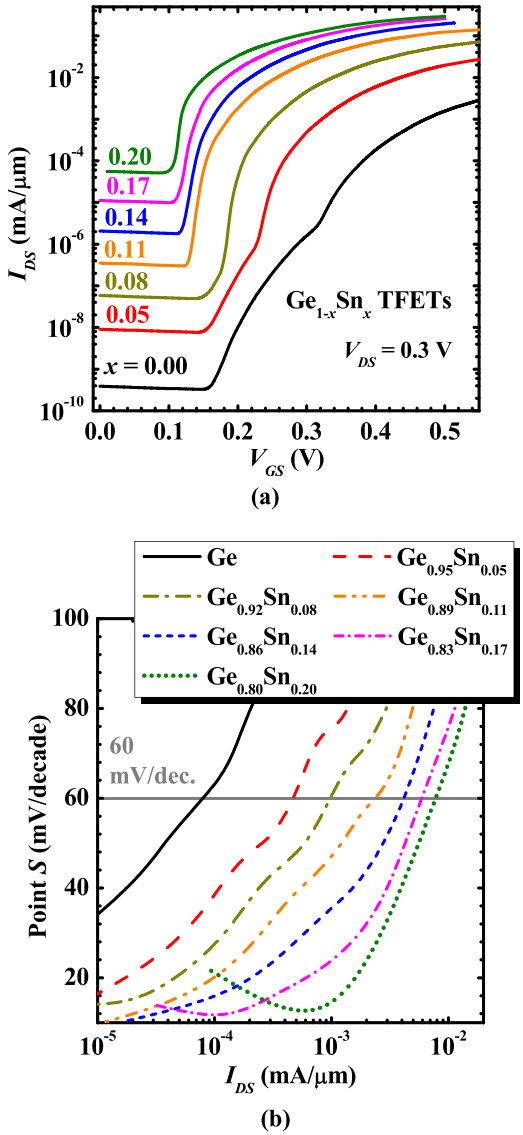

FIG. 8. (a) A set of I_{DS}-V_{GS} curves of $Ge_{1-x}Sn_x$ TFETs with x ranging from 0 to 0.2. (b) Point S versus I_{DS} for $Ge_{1-x}Sn_x$ TFETs with x from 0 to 0.2. For $Ge_{0.8}Sn_{0.2}$ TFET, sub-60 mV/decade S is achieved at a high current level of $\sim 8\ \mu A/\mu m$.

steeper S in comparison with indirect BTBT (Fig. 7). Second, the reduction in band-gap of $Ge_{1-x}Sn_x$ causes enhanced I_{DS} as x increases, leading to the improvement of S especially at high current level. For $Ge_{0.8}Sn_{0.2}$ TFET, sub-60 mV/decade S is achieved at I_{DS} of around 8 $\mu A/\mu m$.

Fig. 9 depicts I_{OFF} versus I_{ON} characteristics for $Ge_{1-x}Sn_x$ TFETs with $x = 0.00$, 0.05, 0.08, 0.11, and 0.17. For a given I_{OFF}, V_{OFF} is the value of V_{GS} when I_{DS} equals to I_{OFF}, and I_{ON} is extracted at $V_{GS} - V_{OFF} = V_{DS} = 0.3$ V. For a given I_{OFF}, $Ge_{1-x}Sn_x$ TFETs demonstrate higher I_{ON} and I_{ON}/I_{OFF} compared to Ge, and the enhancement on I_{ON} and I_{ON}/I_{OFF} becomes larger with increasing x. For $I_{OFF} = 1$ nA/μm, I_{ON} of 0.09 mA/μm and I_{ON}/I_{OFF} of $\sim 10^5$ can be achieved in $Ge_{0.89}Sn_{0.11}$ TFET. In addition, I_{ON} of $Ge_{1-x}Sn_x$ TFET shows less sensitivity to I_{OFF} than that of Ge TFET. This is attributed to the improved S characteristics of $Ge_{1-x}Sn_x$ TFETs as compared to Ge device. It should be noted that for $I_{OFF} = 2 \times 10^{-7}$ mA/μm, I_{ON} of $Ge_{0.98}Sn_{0.08}$

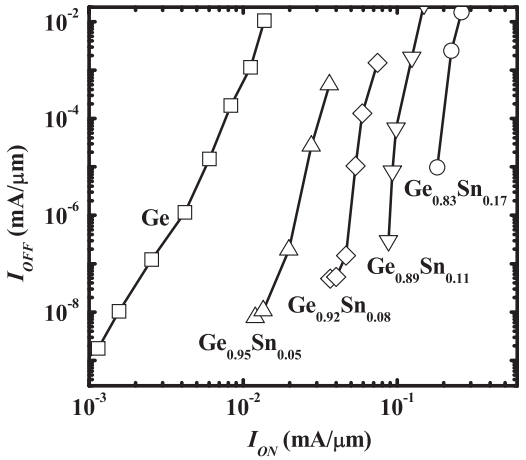

FIG. 9. I_{OFF} versus I_{ON} of $Ge_{1-x}Sn_x$ TFETs with $x = 0.00$, 0.05, 0.08, 0.11, and 0.17 at a supply voltage of 0.3 V. For a given I_{OFF}, V_{OFF} is the value of V_{GS} when I_{DS} equals to the I_{OFF}, I_{ON} is extracted at $V_{GS} - V_{OFF} = V_{DS} = 0.3$ V. I_{OFF} is varied from 10^{-9} to 10^{-2} mA/μm. For a fixed I_{OFF}, I_{ON} of $Ge_{1-x}Sn_x$ TFET is higher than that of Ge TFET.

TFET is about 1 order of magnitude higher than that in Ge TFET. Ref. 57 used a self-consistent non-equilibrium Green's Function Method–Poisson Equation transport simulator to study the $Ge_{0.925}Sn_{0.075}$ TFET, and also observed $\sim$10 times I_{ON} enhancement over Ge TFET at $I_{OFF} = 2 \times 10^{-7}$ mA/μm. Moreover, it was found that relaxed $Ge_{1-x}Sn_x$ TFET with $x > 0.075$ outperforms Ge TFET under 2.5 GPa biaxial tensile stress (Ge becomes direct band-gap at this stress),[57] indicating that GeSn is more promising for TFET application than Ge.

V. CONCLUSION

We performed a simulation study of $Ge_{1-x}Sn_x$ n-channel TFETs with Sn composition varying from 0 to 0.2. The material parameters were extracted from full band structure by EPM calculations, which were subsequently imported to TCAD for device simulation. By increasing Sn composition, I_{ON} of $Ge_{1-x}Sn_x$ TFETs is increased due to the higher direct BTBT rate which relates to the reduction in $E_{G,\Gamma}$. In addition, the maximum I_{DS} with sub-60 mV/decade S becomes higher with increasing Sn composition. For $Ge_{0.8}Sn_{0.2}$ TFET, sub-60 mV/decade S is achieved at I_{DS} of $\sim 8\ \mu A/\mu m$. For a given I_{OFF}, I_{ON} of $Ge_{1-x}Sn_x$ TFETs with x higher than 0.11 is higher than that of Ge TFET at a supply voltage of 0.3 V.

ACKNOWLEDGMENTS

Research grant from the National Research Foundation (NRF) (Award number NRF-RF2008-09), Singapore is acknowledged.

[1]J. Appenzeller, Y.-M. Lin, J. Knoch, and Ph. Avouris, Phys. Rev. Lett. **93**, 196805 (2004).
[2]K. Jeon, W.-Y. Loh, P. Patel, C. Y. Kang, J. Oh, A. Bowonder, C. Park, C. S. Park, C. Smith, P. Majhi, H.-H. Tseng, R. Jammy, T.-J. K. Liu, and C. Hu, in *2010 Symposium on VLSI Technology (VLSIT)*, 15–17 June 2010 (IEEE, 2010), pp. 121–122.
[3]D. Leonelli, A. Vandooren, R. Rooyackers, A. S. Verhulst, S. D. Gendt, M. M. Heyns, and G. Groeseneken, Jpn. J. Appl. Phys. **49**, 04DC10 (2010).

[4]R. Gandhi, Z. Chen, N. Singh, K. Banerjee, and S. Lee, IEEE Electron Device Lett. **32**, 1504 (2011).
[5]F. Mayer, C. Le Royer, J.-F. Damlencourt, K. Romanjek, F. Andrieu, C. Tabone, B. Previtali, and S. Deleonibus, in *IEEE International Electron Devices Meeting*, 15–17 December 2008 (IEEE, 2008), pp. 1–5.
[6]T. Krishnamohan, D. Kim, S. Raghunathan, and K. C. Saraswat, in *IEEE International Electron Devices Meeting*, 15–17 December 2008 (IEEE, 2008), pp 1–3.
[7]S. Mookerjea, D. Mohata, R. Krishnan, J. Singh, A. Vallett, A. Ali, T. Mayer, V. Narayanan, D. Schlom, A. Liu, and S. Datta, in *IEEE International Electron Devices Meeting*, 7–9 December 2009 (IEEE, 2008), pp. 1–3.
[8]G. Han, P. Guo, Y. Yang, C. Zhan, Q. Zhou, and Y.-C. Yeo, Appl. Phys. Lett. **98**, 153502 (2011).
[9]D. K. Mohata, R. Bijesh, S. Mujumdar, C. Eaton, R. Engel-Herbert, T. Mayer, V. Narayanan, J. M. Fastenau, D. Loubychev, A. K. Liu, and S. Datta, in *IEEE International Electron Devices Meeting*, 5–7 December 2011 (IEEE, 2011), pp. 33.5.1–33.5.4.
[10]G. Dewey, B. Chu-Kung, J. Boardman, J. M. Fastenau, J. Kavalieros, R. Kotlyar, W. K. Liu, D. Lubyshev, M. Metz, N. Mukherjee, P. Oakey, R. Pillarisetty, M. Radosavljevic, H. W. Then, and R. Chau, in *IEEE International Electron Devices Meeting*, 5–7 December 2011 (IEEE, 2011), pp. 33.6.1–33.6.4.
[11]A. S. Verhulst, W. G. Vandenberghe, K. Maex, and G. Groeseneken, J. Appl. Phys. **104**, 064514 (2008).
[12]F. Conzatti, M. G. Pala, D. Esseni, E. Bano, and L. Selmi, in *IEEE International Electron Devices Meeting*, 5–7 December 2011 (IEEE, 2011), pp. 5.2.1–5.2.4.
[13]E. O. Kane, J. Appl. Phys. **32**, 83 (1961).
[14]K.-H. Kao, A. S. Verhulst, W. G. Vandenberghe, B. Sorée, G. Groeseneken, and K. De Meyer, IEEE Trans. Electron Devices **59**, 292 (2012).
[15]S. M. Sze and K. K. Ng, *Physics of Semiconductor Devices*, 3rd ed. (Wiley-Interscience, New Jersey, 2007), Chap. 8, p. 427.
[16]M. E. Kurdi, G. Fishman, S. Sauvage, and P. Boucaus, J. Appl. Phys. **107**, 013710 (2010).
[17]D. W. Jenkins and J. D. Dow, Phys. Rev. B **36**, 7994 (1987).
[18]B. Bouhafs, F. Benkabou, M. Ferhat, B. Khelifa, J. P. Dufour, and H. Aourag, Infrared Phys. Technol. **36**, 967 (1995).
[19]Y. Chibane, B. Bouhafs, and M. Ferhat, Phys. Status Solidi B **240**, 116 (2003).
[20]W.-J. Yin, X.-G. Gong, and S.-H. Wei, Phys. Rev. B **78**, 161203 (2008).
[21]Y. Chibane and M. Ferhat, J. Appl. Phys. **107**, 053512 (2010).
[22]K. A. Mäder, A. Baldereschi, and H. von Känel, Solid State Commun. **69**, 1123 (1989).
[23]Y.-H. Zhu, Q. Xu, W.-J. Fan, and J.-W. Wang, J. Appl. Phys. **107**, 073108 (2010).
[24]P. R. Pukite, A. Harwit, and S. S. Iyer, Appl. Phys. Lett. **54**, 2142 (1989).
[25]J. Piao, R. Beresford, T. Licata, I. Wang, and H. Homma, J. Vac. Sci. Technol. B **8**, 221 (1990).
[26]O. Gurdal, P. Desjardins, J. R. A. Carsson, H. Taylor, H. H. Radamson, J. E. Sundgren, and J. E. Greene, J. Appl. Phys. **83**, 162 (1998).
[27]S. Su, W. Wang, B. Cheng, G. Zhang, W. Hu, C. Xue, Y. Zuo, and Q. Wang, J. Cryst. Growth **317**, 43 (2011).
[28]G. He and H. A. Atwater, Appl. Phys. Lett. **68**, 664 (1996).
[29]Y. Shimura, N. Tsutsui, O. Nakatsuka, A. Sakai, and S. Zaima, Thin Solid Films **518**, S2 (2010).
[30]M. R. Bauer and J. Tolle, Solid State Commun. **127**, 355 (2003).
[31]C. S. Cook, S. Zollner, M. R. Bauer, P. Aella, J. Kouvetakis, and J. Menéndez, Thin Solid Films **455**, 217 (2004).
[32]B. Vincent, F. Gencarelli, H. Bender, C. Merckling, B. Douhard, D. H. Petersen, O. Hansen, H. H. Henrichsen, J. Meersschaut, W. Vandervorst, M. Heyns, R. Loo, and M. Caymax, Appl. Phys. Lett. **99**, 152103 (2011).
[33]G. He and H. A. Atwater, Phys. Rev. Lett. **79**, 1937 (1997).
[34]H. P. L. de Guevara, A. G. Rodríguez, H. Navarro-Contreras, and M. A. Vidal, Appl. Phys. Lett. **84**, 4532 (2004).
[35]V. R. D'Costa, C. S. Cook, A. G. Birdwell, C. L. Littler, M. Canonico, S. Zollner, J. Kouvetakis, and J. Menéndez, Phys. Rev. B **73**, 125207 (2006).
[36]R. Chen, H. Lin, Y. Huo, C. Hitzman, T. I. Kamins, and J. S. Harris, Appl. Phys. Lett. **99**, 181125 (2011).
[37]G. Han, S. Su, C. Zhan, Q. Zhou, Y. Yang, L. Wang, P. Guo, W. Wang, C. P. Wong, Z. X. Shen, B. Cheng, and Y.-C. Yeo, in *IEEE International Electron Devices Meeting (IEDM)*, 5–7 December 2011 (IEEE, 2011), pp. 16.7.1–16.7.3.
[38]S. Gupta, R. Chen, B. Magyari-Köpe, H. Lin, B. Yang, A. Nainani, Y. Nishi, J. S. Harris, and K. C. Saraswat, in *IEEE International Electron Devices Meeting (IEDM)*, 5–7 December 2011 (IEEE, 2011), pp. 16.6.1–16.6.4.
[39]G. Han, S. Su, L. Wang, W. Wang, X. Gong, Y. Yang, Ivana, P. Guo, C. Guo, G. Zhang, J. Pan, Z. Zhang, C. Xue, B. Cheng, and Y.-C. Yeo, in *2012 Symposium on VLSI Technology (VLSIT)*, 12–14 June 2012 (IEEE, 2012), pp. 97–98.
[40]S. Gupta, B. Vincent, D. Lin, M. Gunji, A. Firrincieli, F. Gencarelli, B. Magyari-Köpe, B. Yang, B. Douhard, J. Delmotte, A. Franquet, M. Caymax, J. Dekoster, Y. Nishi, and K. C. Saraswat, in *2012 Symposium on VLSI Technology (VLSIT)*, 12–14 June 2012 (IEEE, 2012), pp. 95–96.
[41]M. L. Cohen and T. K. Bergstresser, Phys. Rev. **141**, 789 (1966).
[42]K. L. Low, Y. Yang, G. Han, W.-J. Fan, and Y.-C. Yeo, J. Appl. Phys. **112**, 103715 (2012).
[43]A. Baldereschi and N. O. Lipari, Phys. Rev. B **8**, 2697 (1973).
[44]E. O. Kane, J. Phys. Chem. Solids **12**, 181 (1960).
[45]C. Shen, L.-T. Yang, G. Samudra, and Y.-C. Yeo, Solid-State Electron. **57**, 23 (2011).
[46]L. Brillouin, C. R. Acad. Sci. **183**, 24 (1926).
[47]G. Wentzel, Z. Phys. **38**, 518 (1926).
[48]H. A. Kramers, Z. Phys. **39**, 828 (1926).
[49]*Sentaurus Device User Guide* (Synopsys, Inc., Mountain View, CA, 2011), Version F-2011.09.
[50]A. G. Chynoweth, R. A. Logan, and D. E. Thomas, Phys. Rev. **125**, 877 (1962).
[51]M. Luisier and G. Klimeck, J. Appl. Phys. **107**, 084507 (2010).
[52]D. M. Caughey and R. E. Thomas, Proc. IEEE **55**, 2192 (1967).
[53]S. Selberherr, Microelectron. Reliab. **24**, 225, (1984).
[54]L. Huldt, N. G. Nilsson, and K. G. Svantesson, Appl. Phys. Lett. **35**, 776 (1979).
[55]R. Häcker and A. Hangleiter, J. Appl. Phys. **75**, 7570 (1994).
[56]W. Shockley and W. T. Read, Jr., Phys. Rev. **87**, 835 (1952).
[57]R. Kotlyar, U. E. Avci, S. Cea, R. Rios, T. D. Linton, K. J. Kuhn, and I. A. Young, Appl. Phys. Lett. **102**, 113106 (2013).